Shape-memory NiTi–Nb foams

Ampika Bansiddhi
Department of Materials Engineering, Kasetsart University, Bangkok 10900, Thailand

David C. Dunand[a)]
Department of Materials Science and Engineering, Northwestern University, Evanston, Illinois 60208

A new powder metallurgy technique for creating porous NiTi is demonstrated, combining liquid phase sintering of prealloyed NiTi powders by Nb additions and pore creation by NaCl space-holders. The resulting foams exhibit well-densified NiTi–Nb walls surrounding interconnected pores created by the space-holder, with controlled fraction, size, and shape. Only small amounts of Nb (3 at.%) are needed to produce a eutectic liquid that considerably improves the otherwise poor densification of NiTi powders. NiTi–Nb foams with 34–44% porosity exhibit high compressive failure stress (>1,500 MPa), ductile behavior (>50% compressive strain), low stiffness (10–20 GPa), and large shape-memory recovery strains. These thermomechanical properties, together with the known biocompatibility of the alloy, make these open-cell foams attractive for bone implant applications.

I. INTRODUCTION

Porous, near-equiatomic nickel-titanium (NiTi) alloys have attracted attention for use in multifunctional applications, such as actuators and biomedical implants, due to the combination of unusual properties of NiTi (shape-memory and superelastic properties, high strength, good impact resistance and damping, high corrosion resistance, and excellent biocompatibility[1]) and the lower density and stiffness and higher surface area offered by the porosity. Various methods exist to create porous NiTi: conventional powder-metallurgy (PM) techniques [such as conventional sintering in vacuum or argon,[2,3] self-propagating high-temperature synthesis (SHS),[4–6] capsule-free hot isostatic pressing (HIP)[7]], solid-state foaming by expansion of argon bubbles,[8,9] or continuous zone melting with hydrogen gas evolution during solidification.[10] However, control over pore fraction, size, shape, and connectivity relies mostly on processing parameters and initial powder packing. Tailor-made porous structures are achieved only with difficulty, and processing windows are narrow for these methods.

Various temporary space-holders have been added to prealloyed NiTi (or elemental Ni and Ti) powders to create, after densification and removal, NiTi foams with pores of controlled fraction, size, and shape: saccharose, polymethyl methacrylate, and sodium chloride in HIP or metal injection molding (MIM)/sintering,[11] sodium chloride,[12] and sodium fluoride[13] in HIP, and ammonium bicarbonate in sintering and capsule-free HIP.[14,15] How-

ever, residual microporosity in the NiTi walls surrounding the pores, due to insufficient densification, is usually observed. This microporosity can affect the mechanical properties and other performance indices of the foams; in bone implant, for example, pores smaller than 50 μm are not filled by bone ingrowth.[16]

Although pressure-assisted densification by HIP followed by extended high-temperature sintering have been used to create NiTi foams with NaCl space-holders,[12] poor densification of the NiTi powders could not be overcome. Using elemental Ni and Ti powders as starting materials can enhance densification, due to the high temperature produced by the exothermic NiTi synthesis reaction, but often leads to undesirable secondary phases found in the processing of monolithic NiTi[17,18] and porous NiTi.[14,19]

Transient liquid phase sintering is another option to enhance densification of powders forming a walls or struts of foams, as demonstrated for foams of a nickel-based superalloy: transient liquid bonding of powders on carbon[20] or polymer foam templates,[21] or super-solidus liquid phase sintering of powders in conjunction with a polyoxymethylene space-holder.[22] Near-dense structures were achieved in the cell walls/struts while, in the latter case, pore structure nearly replicates the geometry of the space-holders. Although this method has not yet been used to create NiTi foams from powders, there are many examples where reactive eutectic brazing was used to join NiTi to itself, e.g., pure Cu and Ti–15Cu–15Ni foil with infrared vacuum brazing,[23] Ag–Ti and Ag–Cu–Ti alloys with microwave brazing,[24] and pure Nb under vacuum heating.[25,26] In the latter study, Grummon and co-workers[25] brazed Ni-rich NiTi strips

to create honeycomb structures by creating a eutectic at 1170 °C (140 °C below the melting point of NiTi). They showed that the solidified braze consists of two phases (NiTi and Nb, with little mutual solubility) and does not fail even after extensive superelastic deformation of the honeycomb in compression.

Translating the previous results[26] from NiTi strips to NiTi powders, Nb is an interesting so far unexplored candidate to perform transient liquid sintering on NiTi powders. Furthermore, sodium chloride (NaCl) can be used as a space-holder to create porosity in NiTi, since Nb is not expected to react with NaCl, given that the free energy of formation of $NbCl_5$ is much smaller than that of NaCl.[27]

NiTi–Nb alloys produced by powder metallurgy are novel as all previous reports (except, to our knowledge, Ref. 28) of such alloys used liquid processing approaches, such as arc- or induction-melting followed by casting. Although previous studies of these NiTi–Nb alloys have focused on the shape-memory properties for coupling/joint applications,[29–33] or more recently, on hydrogen dissolution and diffusion in membranes for hydrogen purification,[34–36] biomedical implant applications (such as stents[37,38]) are another promising use for these alloys. In fact, a NiTi–Nb alloy with $Ti_{44}Ni_{47}Nb_9$ composition prepared by arc-melting was found to develop passive oxide layers imparting high corrosion resistance when tested in simulate body fluid.[39] Furthermore, pure niobium exhibits excellent biocompatibility and is nontoxic in tissue interaction.[40] An additional advantage of Nb additions to NiTi for such applications is the improved radiopacity of the alloy.

In this work, we demonstrate a new PM technique for porous NiTi, which combines (i) eutectic liquid sintering of NiTi powders with Nb additions to ensure high densification of NiTi walls and eliminate undesirable micropores; and (ii) the use of NaCl space-holder to create and control the structure of macropores. The microstructure, phase transformation, and mechanical behavior of these NiTi–Nb foams are found to be favorable for applications such as biomedical implants.

II. EXPERIMENTAL PROCEDURES

A. Materials and processing methods

Prealloyed NiTi powders were used to prevent the undesirable nonequiatomic Ni–Ti phases often present when elemental powders are reacted, and also to prevent the formation of high melting Ni–Nb intermetallic phases that may prevent the formation of the low-melting eutectic NiTi–Nb phase. Prealloyed NiTi powders (48.6 at.% Ni, from Special Metals Corp., NY) were sieved to a 44–63-μm particle size. Nb powders (99.8% purity, from Alfa Aesar, MA) with a much finer 1–5-μm particle size were mechanically blended with the NiTi powders, for an

average composition of 3.1 at.% Nb and 96.9 at.% NiTi (or 5.3 wt% Nb and 94.7 wt% NiTi), in a twin-shell dry blender for 2 h. NaCl was selected for the space-holder material, as it has low toxicity, is easily eliminated by evaporation or liquid dissolution, is unreactive with NiTi, and was successfully used in a previous investigation of porous NiTi,[12] thus providing a direct comparison with existing Nb-free NiTi foams. NaCl powder with cuboidal shape (99.0% purity, from Alfa Aesar, MA) were sieved to 100–250-μm size and added to the mixed NiTi/Nb blend to achieve 40 and 60 vol% NaCl, corresponding to salt/metal volume ratios of 2/3 and 3/2, respectively. The powder blends were further mixed for 2 h and cold pressed in a 12.7-mm-diameter die at a pressure of 350 MPa. A 10-mm-high green pellet of each powder blend was produced. A control pellet (with Nb but without NaCl) was also produced by the same procedure, except that the total mixing time was 2 h. These pellets were sintered at 1185 °C (15 °C above the NiTi–Nb eutectic temperature[25]) for 10 h, resulting in foams labeled NTN0, NTN40, and NTN60, as summarized in Table I.

Two control Nb-free NiTi foams, with 0 and 40 vol% NaCl space-holders, labeled NT0 and NT40, were also created by the same procedures, except for a higher sintering temperature of 1250 °C and a longer sintering time of 36 h. In all cases, the NaCl space-holders melted (the melting point of NaCl is 801 °C) and evaporated during the temperature ramp to the sintering temperature.

B. Microstructural and mechanical characterization methods

After sintering, a disk-shaped sample (3 mm thick) was cut from each cylindrical pellet using a low-speed diamond saw. The cross section was mounted in epoxy resin and polished with 320-μm SiC paper followed by 9-μm diamond paste, and 0.05-μm alumina paste. The line intercept method from scanning electron microscopy (SEM) images was applied to determine average pore size as $1.12L_o/N_{pore}$ where N_{pore} is the number of pores on a drawn line and L_o is the line length. Total and closed porosities were obtained by the Archimedes' method in deionized water and by helium pycnometry, respectively, using 6.45 g/cm^3 for the density of mono-

TABLE I. Composition and porosity of NiTi specimens.

Specimen	Nb fraction in NiTi (at.%)	NaCl fraction in preform (vol%)	Total porosity after sintering (%)	Open porosity after sintering (%)
NT0	0	0	47.0 ± 0.0	46.6 ± 0.1
NT40	0	40	61.3 ± 0.0	60.8 ± 0.3
NTN0	3.1	0	6.3 ± 0.0	1.5 ± 0.5
NTN40	3.1	40	34.0 ± 0.3	32.2 ± 0.6
NTN60	3.1	60	43.7 ± 0.3	42.4 ± 1.3

lithic NiTi[41] and 6.54 g/cm^3 for that of monolithic NiTi–Nb (3 at.%). Open porosity was calculated as the difference between total and closed porosity.

Phase transformation behavior was determined on small samples (~20 mg, cut by diamond saw) by differential scanning calorimetry (DSC) using a Perkin-Elmer DSC-7 (Shelton, CT) apparatus with a heating and cooling rate of 10 K/min under nitrogen cover gas. Two DSC cycles (ranging from −60 to 170 °C) were performed consecutively for each sample and the second cycle was used to determine the transformation enthalpy (from integration of the peaks) and the phase-transformation temperatures (A_s, A_f, M_s, and M_f, by using the intercept of extrapolation lines at the highest slope of peaks with those of the baseline). The maximum of each peak was defined as A_p (upon heating) or M_p (upon cooling).

One $3 \times 3 \times 6$ mm^3 parallelepiped specimen was cut from each of the NTN0, NTN40, and NTN60 sintered pellets by electro-discharge machining. To remove any oxides formed during the cutting process, the specimens were polished with 320-μm grit sandpaper. To further eliminate any effect from the heat-affected zone and to obtain a fully martensitic structure, the specimens were annealed for 20 min at 120 °C in air, quenched and held for 20 min at room temperature, immersed for 2 min in liquid nitrogen, and maintained for at least 10 min at room temperature before mechanical testing.

The compressive properties of the specimen were evaluated on a screw-driven load frame using a compression cage with aligning rods to ensure parallelism. The crosshead speed was set at 0.05 mm/min and the crosshead displacement was used to calculate strain, after correction of the machine compliance. Mechanical testing for each specimen followed the following procedures. The specimen was compressed at ambient temperature to a strain of 2%, unloaded, removed from the frame, and heat-treated as above (annealed, quenched to room temperature, and then to liquid nitrogen). The specimen dimensions before loading, after unloading, and after annealing (i.e., at room temperature, before quenching in liquid nitrogen) were measured with a point micrometer with a precision of 1 μm. The load-unload-recovery cycles were then repeated up to consecutive maximum compressive strains of 4%, 6%, and 8%. After heat recovery from the last cycle (8% strain) and heat-treatment, specimens NTN40 and NTN60 were deformed in compression until fracture at a crosshead speed of 0.15 mm/min.

III. RESULT AND DISCUSSION

A. Macrostructure

Cross-sectional micrographs of the Nb-free specimens NT0 and NT40 are shown in Figs. 1(a) and 1(b). Despite a green strength sufficient to handle the cold-pressed powder preform, the NiTi powders in specimen NT0 are poorly densified, with large spaces between particles and few sintering necks visible in Fig. 1(a). Similarly, poor sintering is observed between the powders in specimen NT40 [Fig. 1(b)], which contains a high volume fraction of macropore replicating roughly the shape and size of the NaCl powders. This illustrates that creation of porous NiTi having high fractions of macropores separated by well-densified, strong struts/walls is difficult to achieve by conventional pressureless sintering: the 1250 °C sintering temperature used here cannot be raised significantly, given the NiTi melting temperature of 1310 °C
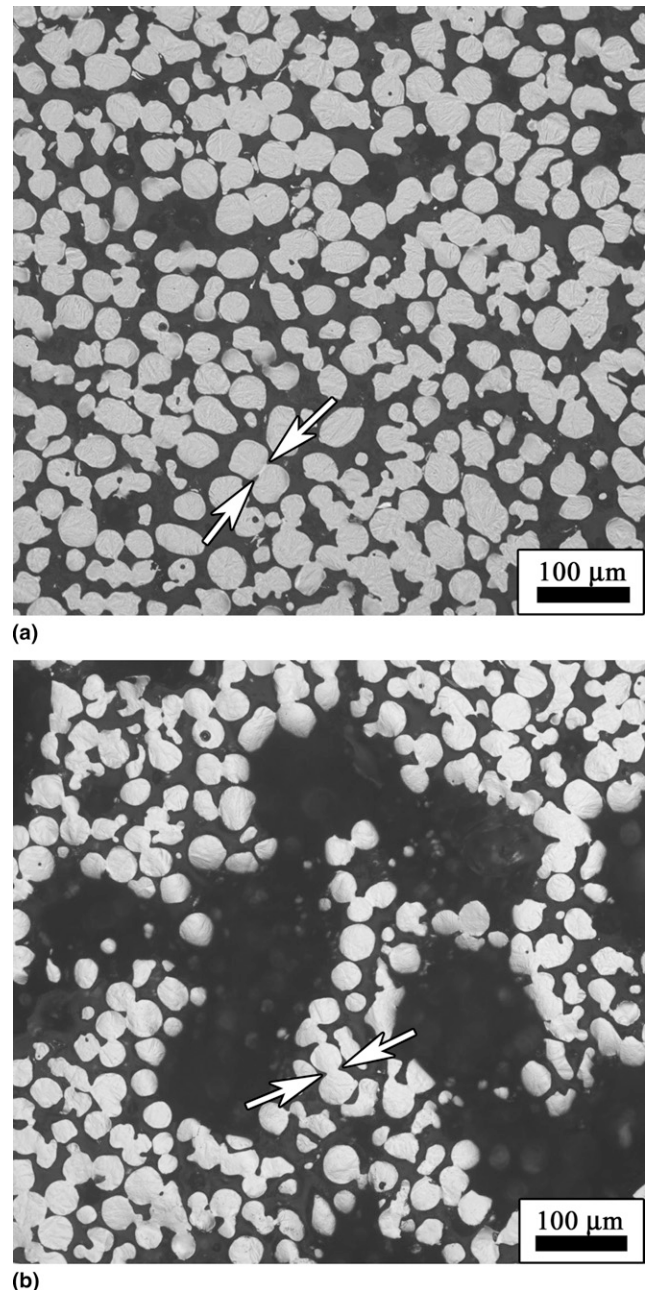

(a)

(b)

FIG. 1. Optical micrographs of NiTi specimens sintered without Nb (a) NT0 and (b) NT40. Arrows indicate a sintering neck.

and the steeply decreasing solidus lines for off-stoichiometric compositions. The poor powder densification probably reflects the slow diffusion coefficients inherent to intermetallic compounds, and it could be circumvented by reducing the NiTi powder sizes. However, this would increase the amount of oxides on the powders that retard sintering kinetics, alter the Ni/Ti ratio (and thus the transformation temperature), and produce brittle inclusions in the metal.

In contrast, the specimens with Nb addition show excellent densification of NiTi powders, with or without space-holders [Figs. 2(a)–2(c)]. This confirms that transient liquid phase sintering slightly above the eutectic temperature enhances densification over solid-state sintering. Upon heating above the eutectic temperature (1170 $^\circ$C[25]), the fine Nb particles react with the large NiTi particles to form a liquid with near-eutectic composition ($Ni_{38}Ti_{36}Nb_{26}$[42] or $Ni_{40}Ti_{40}Nb_{20}$[43]). Capillary forces in the narrow channels between the NiTi particles drive liquid infiltration throughout nearly the entire specimen. Both dissolution and infiltration by wetting may occur concurrently. Furthermore, the liquid phase may allow powder rearrangement leading to local densification in the cell walls.

For control specimen NTN0 [Fig. 2(a)] with no NaCl space-holder, the NiTi matrix achieved a high degree of densification compared to Nb-free specimen NT0 [Fig. 1(a)] whose continuous network of porosity between particles (total porosity of 47%) is eliminated. A small amount of residual porosity (6%, Table II) is present in specimen NTN0 in the form of rounded, equiaxed pores 10–30 μm in size, some of which are merged into elongated pore clusters (50–80 μm in size), distributed evenly at the prior particle junctions in the preform. This small amount of residual closed porosity in control specimen NTN0 may be due to local concentrations of initial porosity in the green compact and/or insufficient liquid formed during sintering. In the former case, the NiTi and Nb particles could be more closely packed during cold pressing (by increasing the pressure) to reduce the size of pores in the green compact and hence increase the capillary forces; the same result could be achieved with smaller NiTi particles, but this approach may lead to increased oxide content as discussed previously. If an insufficient amount of liquid was formed, a simple solution is to use a higher fraction of Nb powder (i.e., >3 at.% Nb). Increasing the amount of liquid is however limited by eventual slumping and distortions of the NiTi specimen. These approaches toward fully dense NiTi were not further studied, since the principal aim of the present study was to create macroporous NiTi.

The two Nb-containing foams with NaCl space-holders, i.e., NTN40 [40 vol% NaCl, Fig. 2(b)] and NTN60 [60 vol% NaCl, Fig. 2(c)], display a homogeneous distribution of macropores with sizes (100–300 μm) and shapes
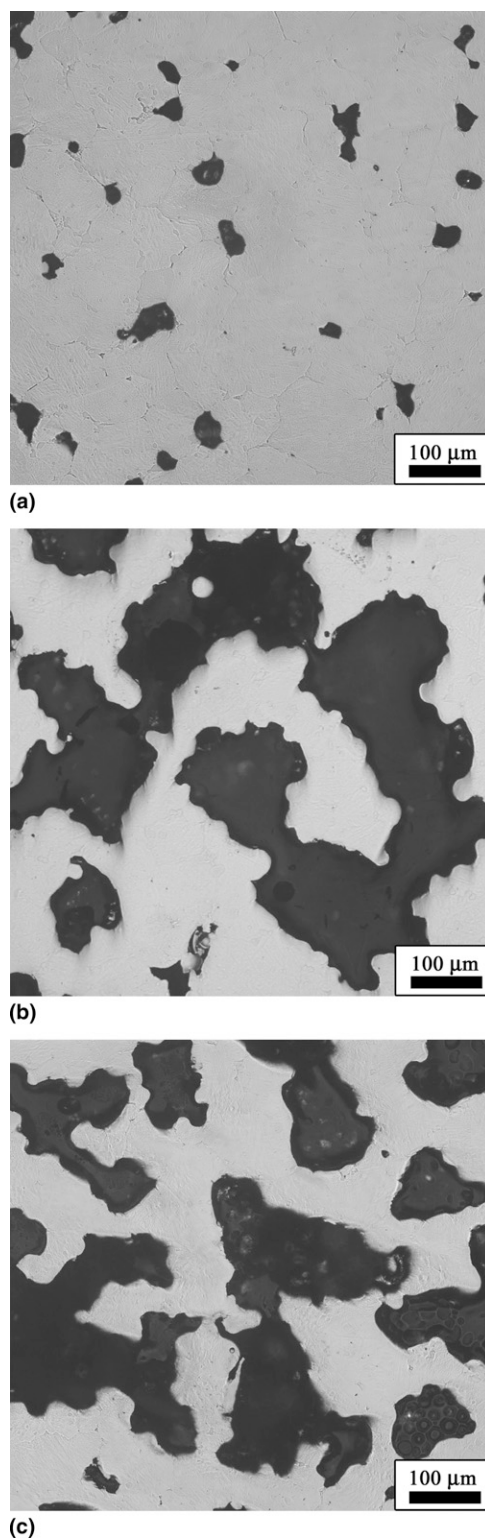

(a)

(b)

(c)

FIG. 2. Optical micrographs of NiTi specimens sintered with Nb (a) NTN0 (6% porosity), (b) NTN40 (34% porosity), and (c) NTN60 (44% porosity).

similar to those of the original NaCl particles. The macropores have good connectivity with each other and their surface is relatively smooth but with numerous dimples

TABLE II. Phase transformation parameters of NiTi specimens.

Specimen	Heat of transformation (J/g)		Transformation temperatures (°C)				Transformation hysteresis/intervals (°C)		
	Heating	Cooling	A_s	A_f	M_s	M_f	A_p–M_p	A_f–A_s	M_s–M_f
NT0	22.6	21.6	75	90	54	35	42	25	19
NT40	26.0	26.4	63	85	50	35	45	22	15
NTN0	16.7	16.1	47	76	31	−21	55	29	52
NTN40	13.0	14.1	31	65	14	−39	70	34	53
NTN60	13.7	14.3	33	65	16	−42	70	32	58

reflecting the shape of individual NiTi particles. The total porosity of the two foams (34% for NTN40 and 44% for NTN60) is significantly lower than the volume fraction of the NaCl space-holder initially added to the powder mixture (40% and 60%, respectively), as expected if the capillary forces from the liquid phase densified the preforms, and/or if some of the liquid phase penetrated into the macropores. However, it is apparent that the capillary forces in the micropores between NiTi particles prevented the transient liquid from filling the large pores created by NaCl removal. The small amounts of microporosity (5%) existing in specimen NTN0 are not present in the foams NTN40 and NTN60: the NiTi walls separating the macropores appear fully dense, as confirmed by the measurement of zero closed porosity of these foams, within experimental error (Table I). This may be because the occasional micropore in the foam is always near enough a macropore to connect to it.

For comparison, the microstructure of a NiTi foam with 32% porosity, produced by hot isostatic pressing of NiTi powders with 40 vol% NaCl at 1065 °C for 4 h, followed by sintering (as well as salt removal) at 1250 °C for 4 h was considered.[12] The present foam NTN60 (with similar pore fraction) has the same range of pore size and porosity as the earlier foams, but higher connectivity, a larger ratio of fenestration to pore size (as qualitatively assessed from the micrographs), and smoother pore surfaces. These improvements are achieved despite the fact that the present method is simpler (no encapsulation and no pressure), operates at lower temperature (1185 versus 1250 °C) in a single step (as opposed to the two HIP and sinter steps). While the effect of processing time was not studied here, it is likely that the present method could be faster as well (i.e., <8 h at temperature). This is because formation of the transient liquid is expected to be rapid with the fine Nb powders and transport in the liquid state is fast, unlike the slow powder densification occurring by solid-state diffusion in conventional sintering.

B. Microstructure

As shown in SEM pictures in Figs. 3(a) and 3(b) for specimens NTN0 and NTN40, respectively, the spherical shape of the NiTi powders are clearly distinguishable and
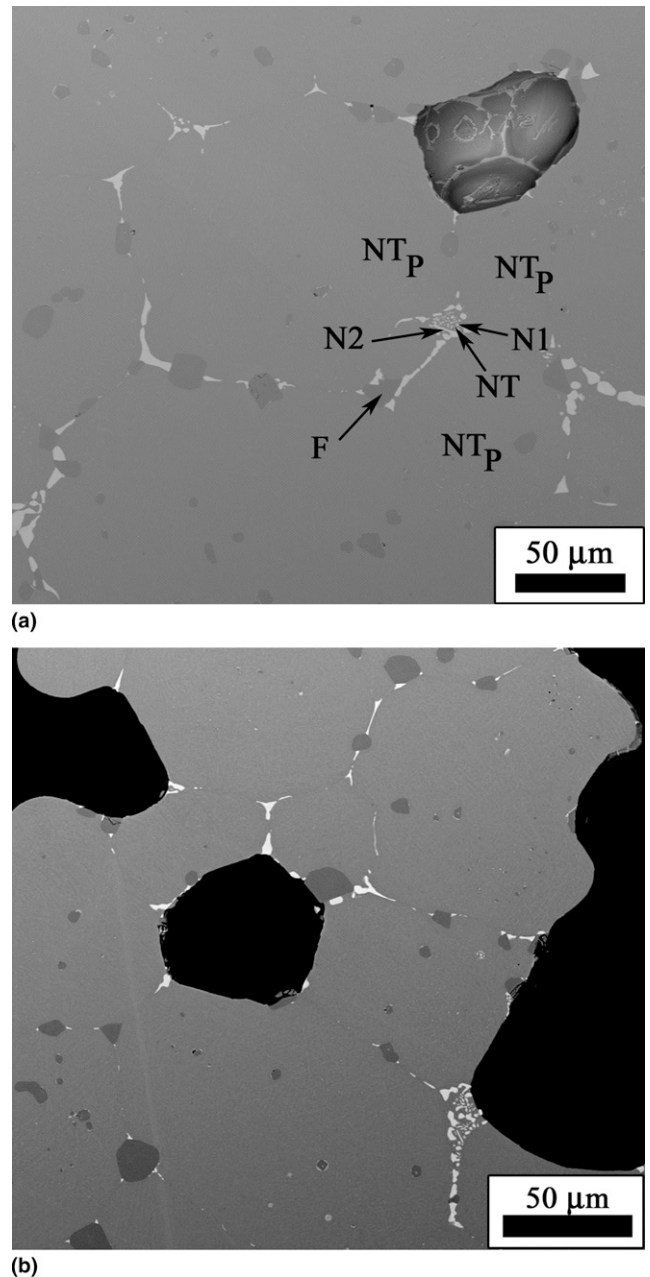

(a)

(b)

FIG. 3. SEM micrographs of (a) specimen NTN0 and (b) NTN40. Gray areas are NiTi particles (NT$_P$) undissolved during sintering or NiTi matrix (NT) in eutectic phase. Brighter regions are Nb-rich phase in eutectic phase, which are either elongated (N1) or blocky (N2). Darker faceted-shape particles are NiTi$_2$ phases (F). Pores are filled with black epoxy resin in (b), but not in (a).

these powders are bonded by a solidified two-phase eutectic. On the basis of the contrast visible in these backscattered micrographs where lighter color indicate a higher atomic mass, the eutectic consists of a matrix (labeled NT) with composition close to NiTi (same color as the undissolved NiTi particles, labeled NT$_P$) and Nb-rich discontinuous phase (lightest color) as shown at higher magnification in Fig. 4(a). This latter phase can have two morphologies: (i) colonies of fine globules (<5 μm), labeled N1, which at times are elongated into lamellae (up to ~40 μm in length), or (ii) large (5–20 μm) isolated
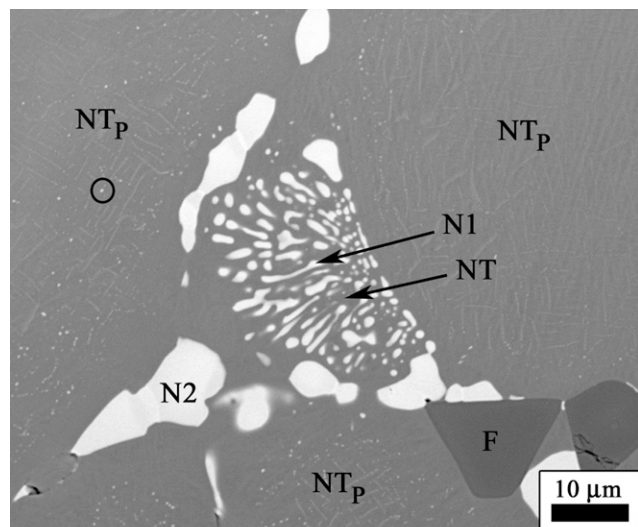
(a)
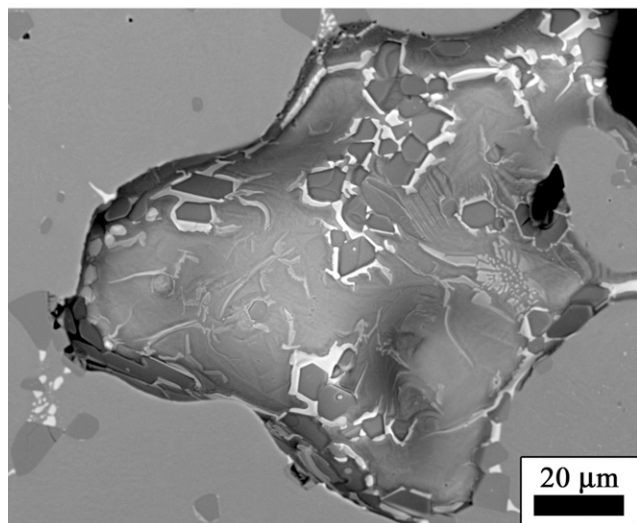
(b)

FIG. 4. SEM micrographs of specimen NTN40 showing microstructure of the solidified transient liquid phases (a) on polished specimen surface and (b) on the inner surface of a pore. In (a), three gray NiTi powders (NT$_P$) are bonded by eutectic phase, consisting of a NiTi matrix (NT) containing bright Nb-rich phase, which are either elongated (N1) or blocky (N2). Darker faceted primary particles (F) are NiTi$_2$ phases. A small Nb-rich precipitate is circled within one of the NiTi powders. The same phases are visible in (b).

rounded or elongated phases labeled N2. This is in good agreement with the microstructure found in induction-melted, near-equiatomic Ni$_{45}$Ti$_{45}$Nb$_{10}$ alloy[29] and Ni$_{45.5}$Ti$_{45.5}$Nb$_9$ alloy.[44] Unlike studies where the whole sample was liquid before solidifying, the present foams only contained a small fraction of liquid whose composition may not have reached global equilibrium. Furthermore, the phases shown and solidification parameters (i.e., cooling rate and temperature gradient) were different, further explaining minor differences in the eutectic structures found here and in prior studies.[30,35]

Also present in the solidified regions, within the eutectic phase described previously, are large facetted precipitates labeled F in Figs. 3(a) and 4(a), which are darker in backscattering SEM than the NiTi matrix and thus have lower atomic mass: energy dispersive x-ray (EDX) analysis confirms that they have NiTi$_2$ composition, with ~4 at.% Nb. According to the ternary phase diagram,[45] the NiTi$_2$ phase is in equilibrium at 900 °C with NiTi (containing some Nb) and a Nb–Ti phase, and these three phases have been observed in cast Ni$_{45}$Ti$_{45}$Nb$_{10}$.[33] Small changes in composition can, however, lead to different phases: in a slightly Ni-richer alloy (i.e., Ni$_{47}$Ti$_{44}$Nb$_9$) both Ti$_3$(Ni,Nb)$_2$[46,47] and (Ni, Nb)$_3$Ti[48] have been reported.

EDX analysis of the undissolved NiTi particles in regions close to the eutectic show a near-equiatomic composition with ~2–3 at.% Nb, probably corresponding to the small light-colored particles (<1 μm) visible in Fig. 4(a) (circled). It is likely that the long processing time at high temperature (1185 °C for 10 h) allows Nb to diffuse into the NiTi particles which then precipitates upon cooling into these fine particles, as also reported by Siegert et al.[44]

Figure 4(b) shows SEM micrographs of the inner surface of a macropore surrounded by NiTi particles bonded by the solidified transient eutectic liquid. Two high-contrast phases (bright Nb–Ti lamellae and dark faceted NiTi$_2$ precipitates) are visible on the whole pore surface and are similar to those observed on a polished cross section. This indicates that the wetting transient liquid not only fills the inter-particle spaces, but also wets the free surfaces surrounding the macropores. Cross sections show that the thickness of this solidified liquid film is very small (<1 μm).

The lamellar Nb-rich and the blocky Ti-rich phases cannot undergo the martensitic transformation exhibited by near-equiatomic NiTi, thus possibly altering recovery behavior, and the Nb in solid solution within NiTi also affects the transformation temperatures, as discussed in the next sections. Therefore, Nb must be added in quantities sufficiently high to enhance sintering but also sufficiently low to maintain the mechanical properties of NiTi. One disadvantage of the presence of Nb is the slight increase in density of the material (although radiopacity
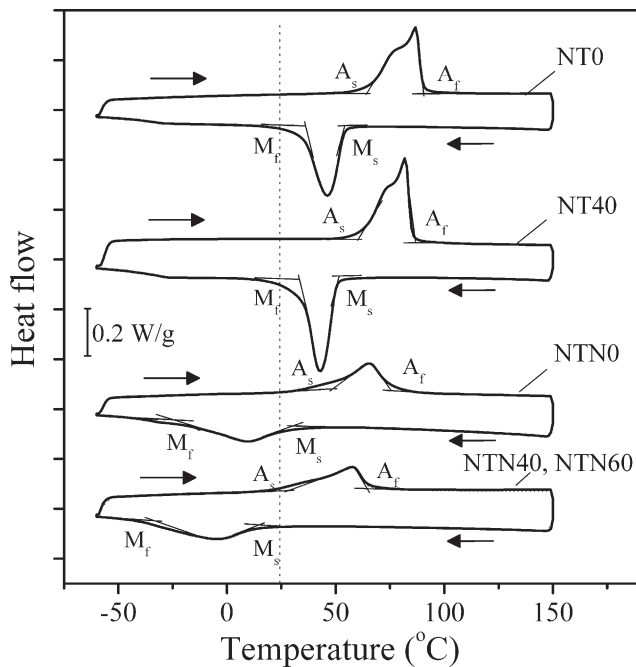
FIG. 5. DSC thermograms of Nb-free specimens NT0 and NT40, and Nb-containing specimens NTN0, NTN40, and NTN60 (the latter two are overlapping).

is concurrently increased), and possibly also its price (although prealloyed NiTi powders are expensive due to the tight control of their composition).

C. Phase transformations

The DSC thermograms for all specimens are shown in Fig. 5 and display the peaks characteristic of the austenite-martensite transformation. The heat of transformation and transformation temperatures (A_s, A_f, M_s, M_f) of each specimen are presented in Table II, which shows that the transformation behavior of the Nb-containing specimens (NTN0, NTN40, and NTN60) differ from the Nb-free specimens (NT0 and NT40) as follows: (i) lower heat of transformation, relative to the literature value for pure NiTi (24 J/g)[41]; (ii) decreased transformation temperatures; (iii) broader martensitic transformation temperature interval (M_s–M_f), and to a lesser extent austenitic transformation interval (A_f–A_s); and (iv) wider peak-to-peak hysteresis (A_p–M_p). At room temperature after heat treatment and quenching to liquid nitrogen, the three Nb-containing specimens should be fully martensitic.

The decrease in heat of transformation is expected to be due to the nontransforming eutectic and precipitate phases, which also produce broadening of the transformation intervals, because they act as obstacles for the transformation in the NiTi. Also, it is known that the addition of Nb increases the local Ni/Ti ratio in the NiTi-rich B2 phase responsible for the recovery effect, and increases the proportion of the Nb-rich phase, which resists transformation

of the B2 phase in the eutectic.[32,43] Therefore, transformation becomes more difficult, and transformation temperatures are decreased. Piao et al.[43] studied the martensitic start temperature (M_s) in NiTi–Nb arc-melted alloys. For both $Ti_{50}Ni_{50-x}Nb_x$ and $Ti_{50-x/2}Ni_{50-x/2}Nb_x$ alloys (to which our alloy belongs), M_s decreases by 20–40 °C for a Nb content of 3 at.%. Uchida et al.[32] reported a decrease in transformation temperature of ~30 °C after adding 3 at.% Nb to equiatomic NiTi produced by vacuum induction melting. This is in general agreement with the decline of M_s by 23 °C from NT0 to NTN0 and by 36 °C from NT40 to NTN40 (Table II). The corresponding decrease of A_s below body temperature for NTN40 and NTN60 may complicate, but not preclude, their use for bone replacement implants, because the foams would be partially transformed when implanted. This may in fact lead to low apparent stiffness, since the foams may exhibit both superelasticity (for the austenitic fraction of the foam) and shape-memory behavior (for the martensitic fraction of the foam).

The thermal behavior of specimens NTN40 and NTN60 display systematic differences with that of NTN0: lower transformation temperatures, broader hysteresis, and reduced heat of transformation. Such differences are not seen between the Nb-free specimens NT0 and NT40, indicating that NaCl alone is not responsible for the effect. One plausible explanation is that the macropores, created by the NaCl particles that have evaporated long before the liquid is created, obstruct the large-scale motion of liquid thus affecting the amount and composition of the liquid and the resulting eutectic and precipitates in the final sintered structure.

D. Thermomechanical behavior

The mechanical behavior during compressive load-unload-recovery cycles is compared in Fig. 6 among the Nb-containing specimens. All specimens survive cycling to a maximum strain of 8% without failure, and display stress plateaus on loading (especially NTN0) and large recovery upon heating after unloading. For NTN0, the stress–strain behavior is comparable with dense, Nb-free NiTi, as can be seen by comparing the curve for NiTi produced by HIP densification of similar prealloyed powders,[49] which is superimposed on the NTN0 cycle to 5% applied strain in Fig. 6(a). Equivalent mechanical behaviors were also reported between dense equiatomic NiTi–Nb alloys (with Nb < 9 at.%) and NiTi alloy in Refs. 32 and 50. The stress plateau on loading of foams NTN40 and NTN60 is indicative of the behavior of foam with well-densified walls, unlike previously reported NiTi foams with less densified walls, which show a near linear loading behavior.[9,12] This is illustrated in Fig. 6(b) by superposing the load-unload cycles for the present foam NTN40 and a foam with less dense walls (produced by HIP followed by NaCl removal,
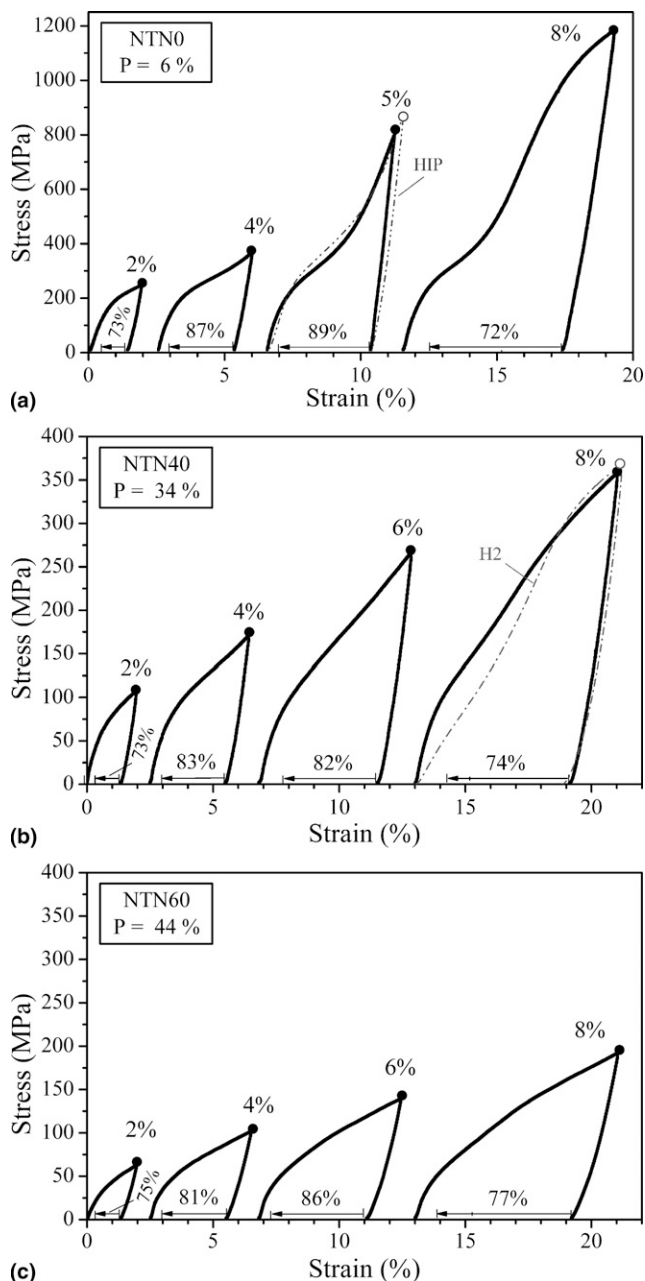
(a)

(b)

(c)

FIG. 6. Series of stress–strain curves for specimens (a) NTN0, (b) NTN40, and (c) NTN60, showing load-unload-recovery cycles with maximum strain of 2%, 4%, 5% (or 6%), and 8%. Curves are shifted along the *x* axis for clarity. Arrows along the *x* axis for each curve represent the thermally recovered shape-memory strain. The published load-unload cycle of a dense NiTi specimen produced by HIP[47] up to a maximum strain of 5% is plotted as a dotted line in (a). Published load-unload cycle of foam H2 (32% porosity) produced by HIP with NaCl followed by NaCl removal[12] is shown as a dotted line in (b).

with the same porosity, and labeled H2[12]). For the present foams, the plateau stress, determined by an interception of initial slope and plateau slope, is ~200 MPa for NTN0, ~80 MPa for NTN40, and ~50 MPa for NTN60. Stresses at the maximum strain of 8% decreased with increasing porosity, as expected.
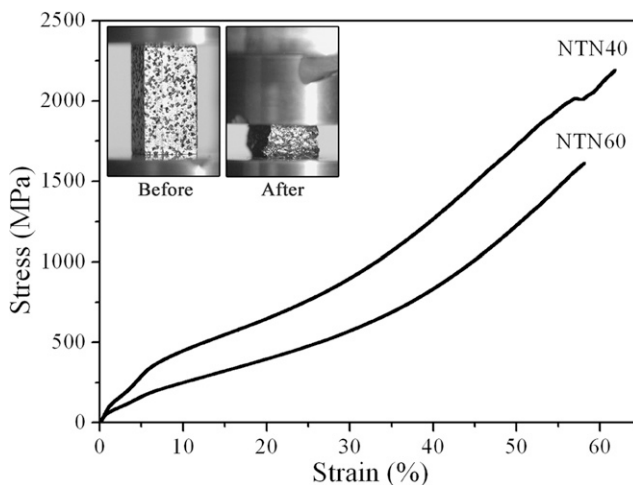

FIG. 7. Compressive stress–strain curves of foams NTN40 and NTN60 deformed up to fracture. Images in inset show foam NTN40 before (left) and after (right) compression.

Upon testing to fracture (Fig. 7), foam NTN40 reached a very high engineering failure stress of 2010 MPa and strain of 57%, while specimen NTN60 achieved 1611 MPa and 58%. The stress–strain curves up to fracture were smooth without serrations or stress drops, up to the first signs of fracture. A macroscopic image (inset in Fig. 7) of specimen NTN40 before and after testing illustrates the ductile behavior of the foam, with extensive plastic deformation and collapse of the cells leading to densification. Accordingly, the energy absorbed during deformation is high, i.e., 96 and 72 J/g for NTN40 and NTN60, respectively, as measured up to a strain of 50%.

Stiffness as a function of maximum cycle strain (determined from curves in Fig. 6) is displayed in Fig. 8. The stiffness on loading is determined from a slope of linear best fit of data between a stress of 10 MPa and a stress 25 MPa below the plateau stress. On unloading, average stiffness is calculated between σ_m–10 and 10 MPa. Specimen NTN0 exhibits increasing stiffness with strain (Fig. 8), which may reflect the densification of the 6% porosity originally present in the specimen. At 8% strain, its unloading stiffness is within the range of values reported in the literature for pore-free NiTi (61–69 GPa).[51] Lower stiffness values on loading are probably due to small amounts of detwinning during loading. The reason for the anomalously high loading stiffness for 5% strain is unclear, but may be linked to texture developing in the specimen from martensite detwinning. Foam specimens NTN40 and NTN60 show much lower stiffness values decreasing with increasing porosity, as expected, and varying little with prestrain. The stiffness values are in the range 10–20 GPa, which is similar to the value for cortical bone.[52] Also, the unloading stiffnesses are ~10 GPa lower than the Gibson-Ashby prediction[52] given by $E = (1 - P)^2 E_{NiTi}$ (27–31 GPa for 34% porosity and 19–22 GPa for 44% porosity). This may be due to a
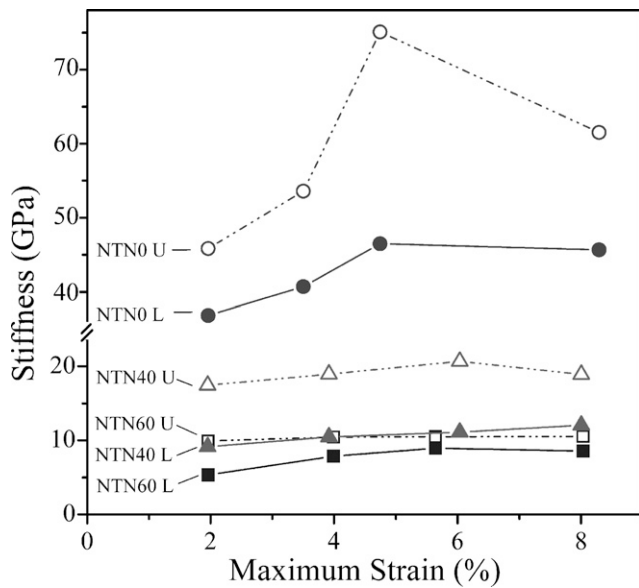
FIG. 8. Loading (L) and unloading (U) stiffness as a function of maximum compressive strain for specimens NTN0, NTN40, and NTN60.

FIG. 9. Unloading, heat recovery, and plastic strain as a function of maximum compressive strain for specimens NTN0, NTN40, and NTN60.

combination of experimental errors, localized detwinning, or even plastic deformation at stress concentrations during unloading (as demonstrated by comparing compressive moduli to ultrasonic measurements in prior NiTi foams[8]), and/or texture developing from incomplete shape-memory recovery. Clearly, composite stiffening by the Nb-rich phases (Nb has a Young's modulus of 105 GPa[53]) does not contribute significantly.

Figure 9 shows, as a function of maximum strain, the unloading, recovery, and plastic strain for all Nb-containing specimens. These strains are respectively defined as the difference of strain at maximum stress and near-zero stress upon unloading, strain before and after heat recovery, and residual strain after heat recovery. Figure 9 shows that the shape-memory, heat recovery strain is larger than the unloading strain and plastic strain, and that all three strains increase linearly with maximum strain. Furthermore, the extent of strain recovery (sum of unloading and heat recovery strain) is independent of porosity (i.e., it is the same for 6%, 34%, and 44% porosity), in agreement with the findings in Ref. 12 for NiTi foams (32–36% porosity) produced by HIP with NaCl space-holders followed by NaCl removal. At 8% maximum applied strain, a total strain of ~6.5% (~2% from unloading and ~4.5% from heat recovery) can be recovered in all specimens, and it is possible that this value may further increase with higher maximum compressive strains. This makes these foams interesting for biomedical applications where unloading and shape-memory strains can be used to deploy the implant within the patients, e.g., for a bone implant expanding to achieve a better fit in a bone cavity.
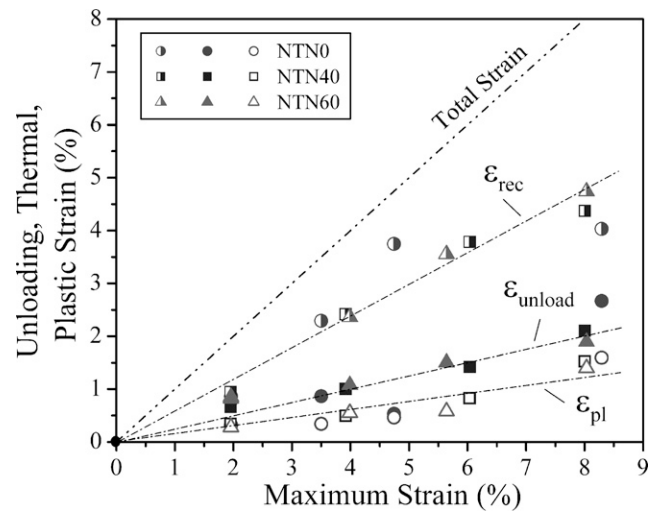
Comparing to a previous NiTi foam with ~32% porosity, produced by HIP and followed by NaCl space-holder removal (labeled H2 in Ref. 12), the present NiTi–Nb foam NTN40 with the same porosity exhibits a comparable strength, a slightly higher stiffness (19 versus 17 GPa), and the same low values of unrecoverable strain (ε_{pl} in Fig. 9) after deformation. Thus, the presence of a nontransformable Nb-rich phase does not impact noticeably the thermomechanical properties of the present foams, while making possible a process without an expensive HIP densification step.

IV. CONCLUSIONS

A novel method for the production of porous NiTi from prealloyed powders was developed, which combines in situ eutectic (NiTi–Nb) liquid sintering and pore formation with transient NaCl space-holder. This method allows (i) the creation of open, interconnected macroporosity, with controllable volume fraction, size, and shape, using NaCl space-holder particles and (ii) the elimination of microporosity present between the NiTi powders forming the walls surrounding the pores, which cannot be removed by conventional sintering of prealloyed NiTi powders.

The resulting NiTi–3 at.% Nb foams have high shape-memory recovery strains, as well as high strength and ductility in compression, while displaying low stiffness. Together with the known biocompatibility of NiTi–Nb alloys, these thermomechanical properties make the present foams particularly interesting for biomedical implants.

REFERENCES

1. K. Otsuka and C.M. Wayman: *Shape Memory Materials* (Cambridge University Press, Cambridge, UK, 1998), p. 284.
2. B.Y. Li, L.J. Rong, and Y.Y. Li: Stress-strain behavior of porous Ni–Ti shape memory intermetallics synthesized from powder sintering. *Intermetallics* **8,** 643 (2000).
3. S.L. Zhu, X.J. Yang, F. Hu, S.H. Deng, and Z.D. Cui: Processing of porous TiNi shape memory alloy from elemental powders by Ar-sintering. *Mater. Lett.* **58,** 2369 (2004).
4. M. Arciniegas, C. Aparicio, J.M. Manero, and F.J. Gil: Low elastic modulus metals for joint prosthesis: Tantalum and nickel-titanium foams. *J. Eur. Ceram. Soc.* **27,** 3391 (2007).
5. C.L. Chu, C.Y. Chung, P.H. Lin, and S.D. Wang: Fabrication of porous NiTi shape memory alloy for hard tissue implants by combustion synthesis. *Mater. Sci. Eng., A* **366,** 114 (2004).
6. B.Y. Li, L.J. Rong, Y.Y. Li, and V.E. Gjunter: Fabrication of cellular NiTi intermetallic compounds. *J. Mater. Res.* **15,** 10 (2000).
7. B. Yuan, M. Zhu, Y. Gao, X. Li, and C.Y. Chung: Forming and control of pores by capsule-free hot isostatic pressing in NiTi shape memory alloys. *Smart Mater. Struct.* **17,** 025013 (2008).
8. C. Greiner, S.M. Oppenheimer, and D.C. Dunand: High strength, low stiffness, porous NiTi with superelastic properties. *Acta Biomater.* **1,** 705 (2005).
9. D.C. Lagoudas and E.L. Vandygriff: Processing and characterization of NiTi porous SMA by elevated pressure sintering. *J. Intell. Mater. Syst. Struct.* **13,** 837 (2002).
10. M. Sugiyama, S.K. Hyun, M. Tane, and H. Nakajima: Fabrication of lotus-type porous NiTi shape memory alloys using the continuous zone melting method and tensile property. *High Temp. Mater. Processes* **26,** 297 (2007).
11. M. Kohl, M. Bram, P. Buchkremer, D. Stover, T. Habijan, and M. Koller: *Production of Highly Porous Near-Net-Shape NiTi Components for Biomedical Applications* (Porous Metals and Metallic Foams Conference, Montreal, QC, Canada, 2007), p. 295.
12. A. Bansiddhi and D.C. Dunand: Shape-memory NiTi foams produced by replication of NaCl sapce-holders. *Acta Biomater.* **4,** 1996 (2008).
13. A. Bansiddhi and D. Dunand: Shape-memory NiTi foams produced by solid-state replication with NaF. *Intermetallics* **15,** 1612 (2007).
14. Y.P. Zhang, D.S. Li, and X.P. Zhang: Gradient porosity and large pore size NiTi shape memory alloys. *Scr. Mater.* **57,** 1020 (2007).
15. Y.P. Zhang, B. Yuan, M.Q. Zeng, C.Y. Chung, and X.P. Zhang: High porosity and large pore size shape memory alloys fabricated by using pore-forming agent (NH_4HCO_3) and capsule-free hot isostatic pressing. *J. Mater. Process. Technol.* **192,** 439 (2007).
16. J.D. Bobyn, R.M. Pilliar, H.U. Cameron, and G.C. Weatherly: The optimum pore-size for the fixation of porous-surfaced metal implants by the ingrowth of bone. *Clin. Orthop. Relat. Res.* **150,** 263 (1980).
17. M. Bram, A. Ahmad-Khanlou, A. Heckmann, B. Fuchs, H.P. Buchkremer, and D. Stover: Powder metallurgical fabrication processes for NiTi shape memory alloy parts. *Mater. Sci. Eng., A* **337,** 254 (2002).
18. A.M. Locci, R. Orru, G. Cao, and Z.A. Munir: Field-activated pressure-assisted synthesis of NiTi. *Intermetallics* **11,** 555 (2003).
19. B. Yuan, X.P. Zhang, C.Y. Chung, M.Q. Zeng, and M. Zhu: A comparative study of the porous TiNi shape-memory alloys fabricated by three different processes. *Metall. Mater. Trans. A* **37,** 755 (2006).
20. D.T. Queheillalt, Y. Katsumura, and H.N.G. Wadley: Synthesis of stochastic open cell Ni-based foams. *Scr. Mater.* **50,** 313 (2004).
21. D.T. Queheillalt, D.D. Hass, D.J. Sypeck, and H.N.G. Wadley: Synthesis of open-cell metal foams by templated directed vapor deposition. *J. Mater. Res.* **16,** 1028 (2001).
22. P. Quadbeck, J. Kaschta, and R.F. Singer: Superalloy IN625 with cellular microstructure: Fabrication route and mechanical properties. *Adv. Eng. Mater.* **6,** 635 (2004).
23. T.Y. Yang, R.K. Shiue, and S.K. Wu: Infrared brazing of $Ti_{50}Ni_{50}$ shape memory alloy using pure Cu and Ti–15Cu–15Ni foils. *Intermetallics* **12,** 1285 (2004).
24. C. van der Eijk, Z.K. Sallom, and O.M. Akselsen: Microwave brazing of NiTi shape with Ag–Ti and Ag–Cu–Ti memory alloy alloys. *Scr. Mater.* **58,** 779 (2008).
25. D.S. Grummon, J.A. Shaw, and J. Foltz: Fabrication of cellular shape memory alloy materials by reactive eutectic brazing using niobium. *Mater. Sci. Eng., A* **438,** 1113 (2006).
26. J.A. Shaw, D.S. Grummon, and J. Foltz: Superelastic NiTi honeycombs: Fabrication and experiments. *Smart Mater. Struct.* **16,** S170 (2007).
27. T.B. Reed: *Free Energy of Formation of Binary Compounds: An Atlas of Charts for High-Temperature Chemical Calculations* (The MIT Press, Cambridge, MA, 1971), p. 81.
28. H.B. Yang, W.H. Ying, Z.P. Yang, J.Y. Lin, X.M. Zhang, and J.H. Guo: Product microstructure of Ti-Ni-Nb shape memory alloy (SMA) by high-temperature synthesis (SHS) of self-propagating. *Rare Metal Mater. Eng.* **31,** 152 (2002).
29. V.Y. Abramov, N.M. Aleksandrova, D.V. Borovkov, S.Y. Makushev, N.A. Polyakova, N.N. Popov, S.D. Prokoshkin, and I.Y. Khmelevskaya: Structure and functional properties of heat-and thermomechanically treated Ti–Ni–Nb-based alloys with a wide martensitic hysteresis. I. Ti–Ni–Nb ternary alloys. *Phys. Met. Metallogr.* **101,** 404 (2006).
30. X.M. He, L.J. Rong, D.S. Yan, Z.M. Jiang, and Y.Y. Li: Study of the $Ni_{41.3}Ti_{38.7}Nb_{20}$ wide transformation hysteresis shape-memory alloy. *Metall. Mater. Trans. A* **35,** 2783 (2004).
31. X.M. He, L.J. Rong, D.S. Yan, and Y.Y. Li: TiNiNb wide hysteresis shape memory alloy with low niobium content. *Mater. Sci. Eng., A* **371,** 193 (2004).
32. K. Uchida, N. Shigenaka, T. Sakuma, Y. Sutou, and K. Yamauchi: Effect of Nb content on martensitic transformation temperatures and mechanical properties of Ti–Ni–Nb shape memory alloys for pipe joint applications. *Mater. Trans.* **48,** 445 (2007).
33. V.A. Udovenko, P.L. Potapov, S.D. Prokoshkin, I.Y. Khmelevskaya, V.Y. Abramov, and Y.V. Blinov: A study of the functional properties of alloy Ti–45% Ni–10% Nb with wide hysteresis of the martensitic transformation. *Metal Sci. Heat Treat.* **42,** 353 (2000).
34. K. Hashi, K. Ishikawa, T. Matsuda, and K. Aoki: Microstructures and hydrogen permeability of Nb–Ti–Ni alloys with high resistance to hydrogen embrittlement. *Mater. Trans.* **46,** 1026 (2005).
35. K. Kishida, Y. Yamaguchi, K. Tanaka, H. Inui, S. Tokui, K. Ishikawa, and K. Aoki: Microstructures and hydrogen permeability of directionally solidified Nb–Ni–Ti alloys with the Nb–NiTi eutectic microstructure. *Intermetallics* **16,** 88 (2008).
36. W. Luo, K. Ishikawa, and K. Aoki: High hydrogen permeability in the Nb-rich Nb–Ti–Ni alloy. *J. Alloys Compd.* **407,** 115 (2006).
37. T. Duerig, D. Stockel, and J. Burpee: Stent. U.S. Patent No. US 6 312 455 B2 (2001).
38. T. Takagi, Y. Sutou, R. Kainuma, K. Yamauchi, and K. Ishida: Effect of prestrain on martensitic transformation in a $Ti_{46.4}Ni_{47.6}Nb_{6.0}$ superelastic alloy and its application to medical stents. *J. Biomed. Mater. Res. B Appl. Biomater.* **76,** 179 (2006).

39. C. Li, Y.F. Zheng, and L.C. Zhao: Electrochemical corrosion behaviour of Ti$_{44}$Ni$_{47}$Nb$_9$ alloy in simulated body fluids. *Mater. Sci. Eng., A* **438,** 504 (2006).

40. H. Matsuno, A. Yokoyama, F. Watari, M. Uo, and T. Kawasaki: Biocompatibility and osteogenesis of refractory metal implants, titanium, hafnium, niobium, tantalum and rhenium. *Biomaterials* **22,** 1253 (2001).

41. C.M. Jackson, H.J. Wagner, and R.J. Wasilewski: *55-Nitinol–The Alloy with a Memory: Its Physical Metallurgy, Properties, and Applications* (National Aeronautics and Space Administration, Washington, DC, 1972).

42. S.B. Prima, L.A. Tretyachenko, and V.M. Petyukh: Phase relations in the Ti–TiNi–NbNi–Nb region of the ternary system Ti–Nb–Ni. *Powder Metall. Met. Ceram.* **34,** 155 (1995).

43. M. Piao, S. Miyazaki, K. Otsuka, and N. Nishida: Effects of Nb addition on the microstructure of Ti–Ni alloys. *Mater. Trans., JIM* **33,** 337 (1992).

44. W. Siegert, K. Neuking, M. Mertmann, and G. Eggeler: Influence of Nb content and processing conditions on microstructure and functional properties of NiTiNb shape-memory alloys. *Mater. Sci. Forum* **394-3,** 361 (2001).

45. S. Matsumoto, T. Tokunaga, H. Ohtani, and M. Hasebe: Thermodynamic analysis of the phase equilibria of the Nb–Ni–Ti system. *Mater. Trans.* **46,** 2920 (2005).

46. C.S. Zhang, Y.Q. Wang, W. Chai, and L.C. Zhao: The study of constitutional phases in a Ni$_{47}$Ti$_{44}$Nb$_9$ shape memory alloy. *Mater. Chem. Phys.* **28,** 43 (1991).

47. L.C. Zhao, T.W. Duerig, S. Justi, K.N. Melton, J.L. Proft, W. Yu, and C.M. Wayman: The study of niobium-rich precipitates in a Ni–Ti–Nb shape memory alloy. *Scr. Metall. Mater.* **24,** 221 (1990).

48. D. Jia, W.X. Liu, Z.Z. Dong, S.J. Yu, Q. Zhang, D.F. Wang, and D.Z. Liu: Precipitations in a Ni Ti–Nb alloy during annealing. *Prog. Nat. Sci.* **9,** 216 (1999).

49. K.L. Fukami-Ushiro and D.C. Dunand: NiTi and NiTi–TiC composites. III: Shape-memory recovery. *Metall. Mater. Trans. A* **27,** 193 (1996).

50. W. Siegert, K. Neuking, M. Mertmann, and G. Eggeler: First cycle shape memory effect in the ternary NiTiNb system. *J. Phys. IV* **112,** 739 (2003).

51. D.C. Dunand, D. Mari, M.A.M. Bourke, and J.A. Roberts: NiTi and NiTi–TiC composites IV: Neutron diffraction study of twinning and shape-memory recovery. *Metall. Mater. Trans. A* **27,** 2820 (1996).

52. L.J. Gibson and M.F. Ashby: *Cellular Solids* (Cambridge University Press, Cambridge, 1997).

53. P. Enghag: *Encyclopedia of the Elements: Technical Data, History, Processing, Applications* (Wiley-VCH, Weinheim, 2004).